Geochimica et Cosmochimica Acta 434 (2026) 153–164

Contents lists available at ScienceDirect

Geochimica et Cosmochimica Acta

journal homepage: www.elsevier.com/locate/gca

Trace-element signatures in magnetite induced by iron-reducing bacteria

Xiaohua Han [a,b,*], James M. Byrne [c], Andreas Kappler [d,e], Wei Lin [a,b], Yongxin Pan [a,b]

[a] Key Laboratory of Planetary Science and Frontier Technology, Institute of Geology and Geophysics, Chinese Academy of Sciences, Beijing 100029, China
[b] College of Earth and Planetary Sciences, University of Chinese Academy of Sciences, Beijing 100049, China
[c] School of Earth Sciences, University of Bristol, Wills Memorial Building, Queens Road, Bristol BS8 1RJ, United Kingdom
[d] Geomicrobiology, Department of Geosciences, University of Tübingen, Schnarrenbergstrasse 94-96, Tübingen 72076, Germany
[e] Cluster of Excellence: EXC 3121, TERRA – Terrestrial Geo-Biosphere Interactions in a Changing World, University of Tübingen, Germany

ARTICLE INFO

Associate Editor: Karim Benzerara

Keywords:
Biogenic magnetite
Dissimilatory iron-reducing bacteria (DIRB)
Trace-element partitioning
Fe redox state

ABSTRACT

Biogenic magnetite nanoparticles produced by microorganisms are ubiquitous in modern environments and likely abundant in ancient sediments such as banded iron formations and paleosols. While magnetotactic bacteria (MTB) synthesize intracellular magnetite with distinctive morphological, chemical, and magnetic biosignatures, dissimilatory Fe(III)-reducing bacteria (DIRB) generate extracellular magnetite that is nanoscale, aggregated, and often superparamagnetic, complicating its distinction from abiotic counterparts. To resolve this challenge, we systematically compared magnetite synthesized through abiotic Fe^{2+}_{aq}-induced ferrihydrite transformation and biogenic transformation mediated by the DIRB *Shewanella oneidensis* MR-1. Ferrihydrite substrates were co-precipitated with 21 trace elements at concentrations of 0, 10, and 20 ppm to evaluate the combined effects of formation pathway and trace-element availability on magnetite particle size, Fe valence state, and trace-element partitioning. Transmission electron microscopy results showed that biogenic magnetite was consistently smaller than abiotic magnetite, with increasing trace-element concentrations further reducing particle size in both systems. Notably, trace elements induced opposite redox trends: abiotic magnetite became progressively oxidized due to substitution-driven Fe^{2+} oxidation, whereas biogenic magnetite became more reduced as microbially mediated Fe(III) reduction was enhanced. Inductively coupled plasma mass spectrometry (ICP-MS) analyses demonstrated distinct trace-element partitioning patterns: abiotic magnetite preferentially incorporated Mg, whereas the biotic solid aggregates were consistently enriched in Co and Cd, regardless of initial trace-element concentrations or post-synthesis washing treatments. Because the biotic solid aggregates contained both magnetite and bacterial biomass, their elemental compositions reflect both mineral and biological pools. Accordingly, our objective is to identify pathway-dependent trace element signatures of biogenic and abiotic magnetite formation rather than to quantify elemental incorporation into a pure magnetite lattice. The observed differences may represent the combined effects of trace-element substitution in the magnetite lattice and biologically mediated processes. Comparison with magnetite produced by MTB further highlights substantial interspecies differences in trace-element partitioning, reflecting how the degree of biological control shapes biomineralization. Collectively, the coupled signatures of particle size, Fe valence distribution, and trace-element partitioning establish a coherent geochemical framework for distinguishing abiotic and biogenic magnetite. These results provide new constraints for identifying extracellular microbial magnetite in modern and ancient sedimentary records, with implications for paleoenvironmental reconstruction and astrobiological exploration.

1. Introduction

Biogenic magnetite nanoparticles produced by microorganisms are widespread in natural environments. These nanoparticles form through intracellular mineralization by magnetotactic bacteria (MTB) or extracellular biomineralization by dissimilatory Fe(III)-reducing bacteria (DIRB), among other pathways. Given that both MTB and DIRB likely originated during the Archean (Lin et al., 2017; Schröder et al., 2003), biogenic magnetite is also expected to persist in ancient sediments such as banded iron formations (BIFs) and paleosols (Han and Pan, 2024; Hua

* Corresponding author at: Key Laboratory of Planetary Science and Frontier Technology, Institute of Geology and Geophysics, Chinese Academy of Sciences, Beijing 100029, China.
E-mail address: hanxiaohua@mail.iggcas.ac.cn (X. Han).

https://doi.org/10.1016/j.gca.2026.10.037
Received 7 April 2026; Accepted 25 October 2026
Available online 26 October 2026
0016-7037/© 2026 Elsevier Ltd. All rights are reserved, including those for text and data mining, AI training, and similar technologies.

et al., 2026). As a potential mineral fossil, biogenic magnetite could provide direct evidence of microbial activity. However, distinguishing biogenic from abiotic magnetite in geological records remains a formidable challenge. To address this, previous studies have proposed diagnostic biosignatures for MTB-derived magnetite, including morphological traits (e.g., size, shape, chain-like arrangements), chemical characteristics (e.g., Fe isotopic compositions, C–N signals, and trace element contents), and magnetic properties (e.g. δ_{FC}/δ_{ZFC}, where δ is the amount of remanence lost by warming through the Verwey transition between the field-cooled (FC) and zero-field cooled (ZFC)) (Amor et al., 2015, 2016; Moskowitz et al., 1993; Pérez-Huerta et al., 2022).

DIRB reduce ferric minerals (e.g., ferrihydrite) by coupling the oxidation of organic compounds, H_2, CH_4, NH_4^+ or sulfide, thereby producing magnetite extracellularly. Unlike the well-defined, single-domain, chain-organized crystals produced by MTB, magnetite formed through DIRB typically occurs as nanometer-sized, superparamagnetic aggregates (Han et al., 2024; Wu et al., 2013). This morphological and magnetic ambiguity complicates its identification in ancient sediments. Consequently, researchers have explored chemical biosignatures for DIRB-derived magnetite. For instance, incubation experiments with *Geobacter sulfurreducens* PCA and *Shewanella putrefaciens* CN32 using goethite and hematite as Fe(III) substrates revealed Fe isotope fractionation between ferric substrates and dissolved Fe(II) (Δ^{56}Fe of −2.95‰ for goethite and −2.70‰ for hematite) that closely resembled those of abiotic systems (−2.9‰ and −3.2‰, respectively) (Crosby et al., 2005, 2007; Wu et al., 2009), limiting their diagnostic utility.

More recently, trace element partitioning has emerged as a promising biosignature. A comparative study demonstrated that DIRB-derived magnetite preferentially incorporates Ni, whereas abiotic magnetite enriches Zn (Han et al., 2021). This differential incorporation arises from the higher Fe^{2+}/Fe^{3+} ratio of DIRB-derived magnetite compared with abiotic magnetite, as Ni^{2+} preferentially substitutes into octahedral Fe^{2+} sites, while Zn^{2+} favors tetrahedral Fe^{3+} sites. These findings suggest that the partition coefficients of trace elements could serve as the proxy for identifying DIRB magnetite in ancient deposits. Nevertheless, further validation under environmentally relevant conditions involving multiple trace elements at variable concentrations remains essential.

The key objective of this study is to quantify the differential partitioning of various trace elements in magnetite formed through abiotic versus biotic pathways. We hypothesize that distinct trace element signatures would emerge under controlled laboratory conditions, providing a robust framework for identifying biogenic magnetite in ancient deposits. We therefore synthesized abiotic magnetite via the reaction of ferrihydrite with dissolved $Fe^{2+}_{(aq)}$, and biogenic magnetite through the secondary transformation of ferrihydrite induced by the DIRB *Shewanella oneidensis* MR-1. The ferrihydrite substrates were co-precipitated with 21 trace elements (Ag, Al, B, Ba, Bi, Ca, Cd, Co, Cr, Cu, Ga, K, Li, Mg, Mn, Na, Ni, Pb, Sr, Tl, Zn) at concentrations of 0, 10, and 20 ppm. The mineralogical and morphologic characteristics of magnetite were analyzed by ^{57}Fe Mössbauer spectroscopy, X-ray photoelectron spectroscopy (XPS), and transmission electron microscopy (TEM). The chemical compositions of different Fe species were quantified by inductively coupled plasma–mass spectrometry (ICP-MS).

2. Materials and methods

2.1. Ferrihydrite substrates, strains and medium

Control ferrihydrite (Fh) without added trace elements was synthesized by reacting pure $Fe(NO_3)_3{\cdot}9H_2O$ (10 g, 99.999%, Sigma-Aldrich, 529303) in 500 mL ultrapure water with KOH (99.99%, Sigma-Aldrich, 306568) until the pH reached 7.0 (Raven et al., 1998). The resulting Fh precipitates were centrifuged (7500 rpm, 10 min) and washed three times with ultrapure water to remove residual nitrate ions. Fh was doped with trace elements during synthesis to simulate naturally occurring Fe(III) (oxyhydr)oxides, which commonly incorporate or adsorb trace elements during precipitation. This experimental design enables evaluation of the redistribution and partitioning of trace elements during the subsequent transformation of ferrihydrite to magnetite under abiotic and biotic conditions. Fh mineral particles co-precipitated with different concentrations of trace elements (0, 10, 20, 30, 40, and 80 ppm) were prepared using a similar procedure, with the addition of 0, 0.5, 1.0, 1.6, 2.1, or 4.2 mL of 1000 mg/L trace element ICP standard solutions (Ag, Al, B, Ba, Bi, Ca, Cd, Co, Cr, Cu, Ga, K, Li, Mg, Mn, Na, Ni, Pb, Sr, Tl, Zn) to the $Fe(NO_3)_3{\cdot}9H_2O$ solution prior to KOH addition. The final trace element concentrations co-precipitated with Fh were determined by ICP-MS. Detailed information on strains and growth media is provided in the Supporting Information.

2.2. Incubation experiments

Both abiotic and biotic experiments were conducted in 50 mL serum bottles containing 25 mL of 30 mM anoxic PIPES (1,4-piperazinediethanesulfonic acid) buffer (pH 7.2) for 18 months. In the abiotic Fh transformation experiments, $Fe^{2+}_{(aq)}$ was reacted with Fh at an Fe^{2+}/Fh molar ratio of 2.5:1 (30 mM $FeCl_2$ and 12 mM Fh), a ratio previously shown to be suitable for magnetite formation (Han et al., 2020). For the biotic Fh transformation experiments, cell suspensions of *S. oneidensis* MR-1 at a concentration of 1.4×10^{10} cells/mL were used to reduce 12 mM Fh with 10 mM lactate as the electron donor. Fh mineral particles co-precipitated with different concentrations of trace elements (0, 10, 20, 30, 40, and 80 ppm) were applied to evaluate the optimal trace element concentrations for magnetite formation. Black precipitates formed in all abiotic experiments regardless of the Fh mineral used. In contrast, in the biotic experiments, black precipitates formed only with Fh co-precipitated with 0, 10, or 20 ppm trace elements, suggesting that higher concentrations (30, 40, 80 ppm) may have been toxic to *S. oneidensis* MR-1. Consequently, subsequent mineral characterization and trace element analyses were performed on the solids from abiotic and biotic experiments using Fh mineral particles with 0, 10, and 20 ppm trace elements. The samples from the biotic experiments contained magnetite together with bacterial cells and potentially cell-associated organic material. Control bottles containing neither $Fe^{2+}_{(aq)}$ nor inoculum were also included.

2.3. Mineral products characterization

For TEM analysis, a drop of slurry was rinsed with ultrapure H_2O to remove residual salts from the medium. The washed samples were placed onto carbon-coated copper grids for characterization of the morphology, particle size, and mineral phases of the final mineral products. TEM imaging was performed on a JEM-2100HR TEM (JEOL, Japan) operated at an acceleration voltage of 200 kV.

For Mössbauer and XPS analyses, mineral products were collected, filtered through 0.45 μm membranes, and dried in an anoxic glovebox. ^{57}Fe Mössbauer spectra at 6 K were recorded using a WSS-10 spectrometer (controlled by Wissoft 2003) with a ^{57}Co/Rh source, and spectra were fitted with MossWinn 4.0. XPS was employed to determine the Fe valence state on magnetite particle surfaces. Measurements were performed on an AXIS Supra X-ray photoelectron spectrometer (Kratos Analytical Ltd.) equipped with a monochromatic Al K_α radiation source. Binding energies were calibrated against the adventitious C 1s peak at 284.8 eV, and background subtraction as well as peak fitting were carried out using the Avantage software.

2.4. Sequential extraction of different Fe species and trace elements analyses

Several Fe species, including aqueous Fe, adsorbed Fe, loosely bound amorphous Fe-bearing precipitates, and crystalline Fe-bearing minerals, were present in the final mineral products. To quantify trace element

concentrations associated with different Fe species, sequential extraction procedures were applied, involving centrifugation and sodium acetate (NaAc) washing (Fig. S1 and Table S1). Bulk samples (4 mL) were collected to represent the total Fe in transformation products (Tp_{tot}). An additional 4 mL aliquot was centrifuged at 12,045×*g* for 10 min, with the supernatant and pellet defined as the aqueous fraction (Tp_{aq}) and solid fraction (Tp_{so}), respectively. A third 4 mL aliquot was centrifuged, and the resulting pellet was washed with anoxic 1 M NaAc (pH ~ 5.0) for 24 h in the dark to dissolve adsorbed Fe and loosely bound amorphous Fe-bearing precipitates (Tp_{NaAc}), while preserving crystalline magnetite under these mild extraction conditions, as confirmed by XRD analysis following the same washing procedure (Han et al., 2021). After

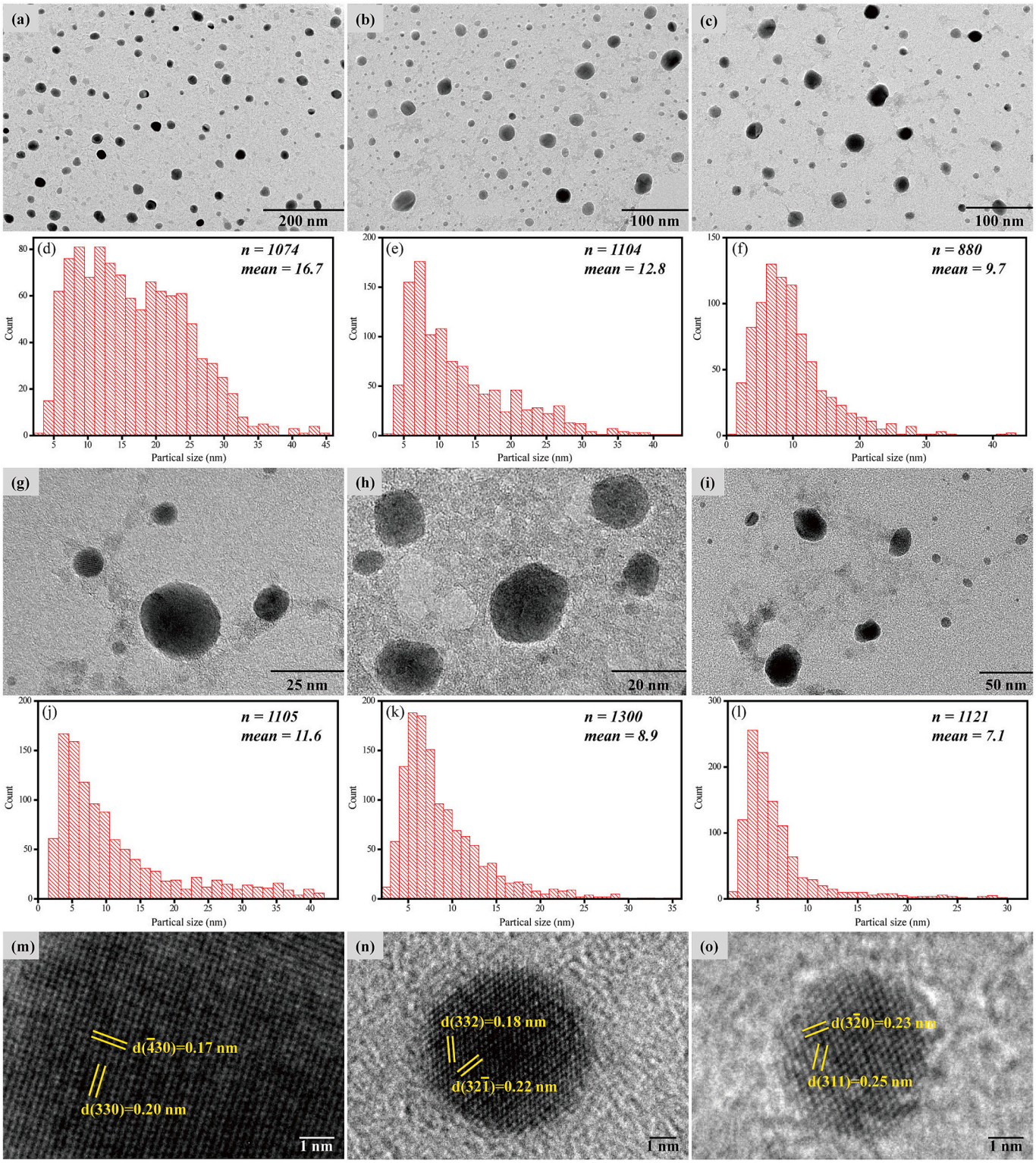


Fig. 1. TEM images and particle size distributions of magnetite formed in abiotic (a–f) and biotic (g–l) experiments. Panels (a, d, g, j) show magnetite transformed from 0 ppm TE-Fh, (b, e, h, k) from 10 ppm TE-Fh, and (c, f, i, l) from 20 ppm TE-Fh. Panels (m–o) present HRTEM micrographs of magnetite formed abiotically from 0 ppm TE-Fh (m) and 20 ppm TE-Fh (n), and biotically from 10 ppm TE-Fh (o).

centrifugation, the remaining precipitates ($Tp_{so\text{-}Ac}$) were digested in 6 M HNO_3. For both abiotic and biotic experiments using the three Fh substrates, all Fe species were prepared in duplicate. All sequential extraction steps were conducted in an anoxic glovebox (100% N_2).

Trace element concentrations of all Fe species (Tp_{tot}, Tp_{aq}, Tp_{so}, Tp_{NaAc} and $Tp_{so\text{-}Ac}$) were determined. Samples were transferred into Teflon beakers and dried on a hot plate at 130°C. The dried residues were digested with 1 mL concentrated HF (22 mol L^{-1}) and 1 mL concentrated HNO_3 (14 mol L^{-1}) at 190°C for 24 h. After evaporation to dryness, the samples were redissolved in 1 mL concentrated HNO_3 and 2 mL ultrapure water (Milli-Q) and heated at 190°C for 12 h. Following a second evaporation step, the final residues were dissolved in 2% ultrapure HNO_3 containing an internal spike of 1 ppm In and subsequently diluted gravimetrically for geochemical analysis. The In internal standard was used to correct for instrumental sensitivity drift during the analytical session and to minimize potential matrix effects arising from variations in sample composition among different samples. The resulting solutions were analyzed by inductively coupled plasma mass

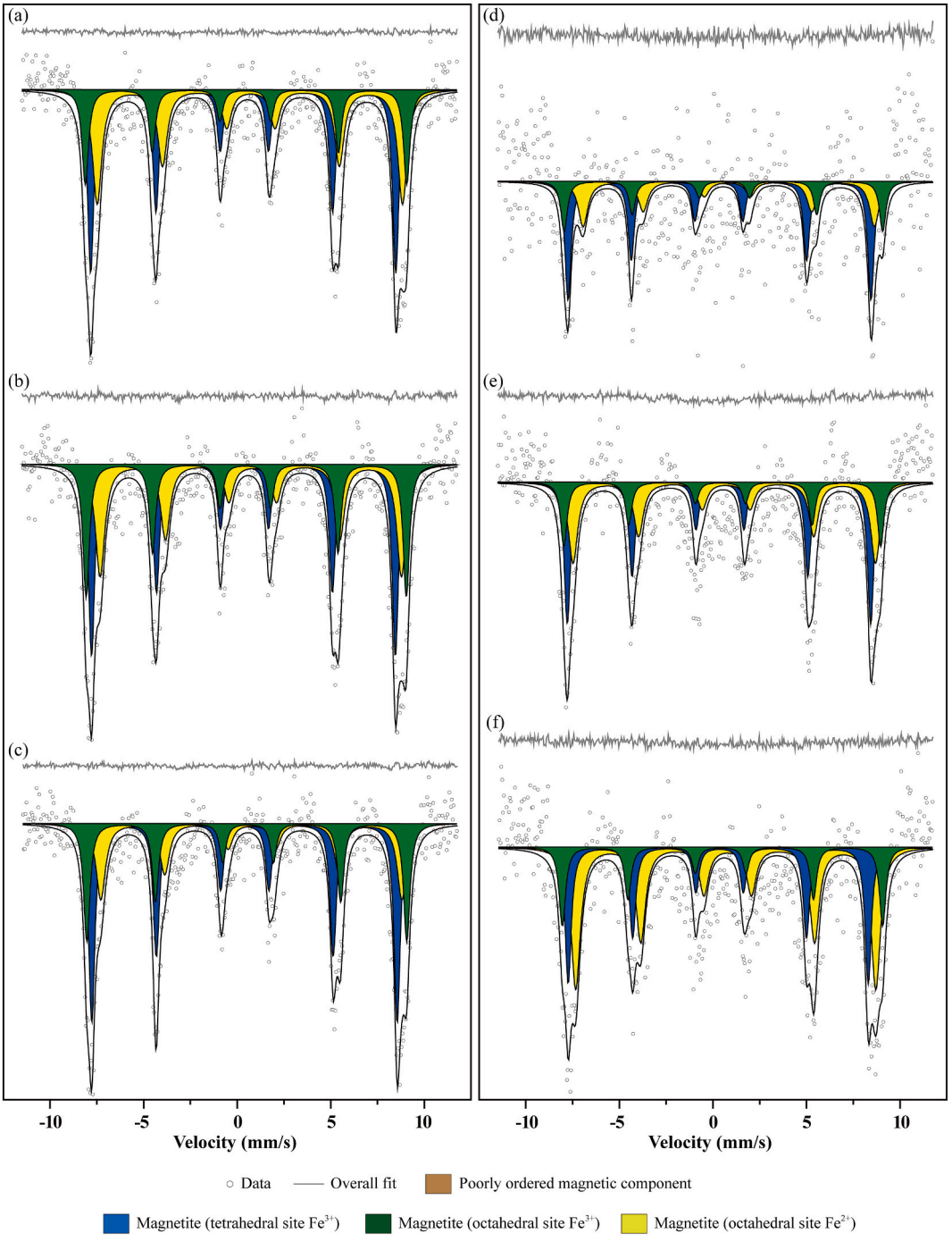


Fig. 2. Mössbauer spectra of transformation products induced by abiotic addition of Fe^{2+}_{aq} (a-c) and biotic reduction by *S. oneidensis* MR-1 (d-f). (a)(d) 0 ppm TE-Fh transformation products; (b)(e) 10 ppm transformation products; (c)(f) 20 ppm transformation products. The relatively high statistical noise mainly reflects counting statistics associated with the limited absorber mass and low Fe content of the samples. The spectra were nevertheless sufficient for phase identification and quantitative fitting, as demonstrated by the 10% residual curves shown above each spectrum. The reduced χ^2 values used to evaluate the fitting quality are summarized in Table S3.

spectrometry (ICP-MS, Agilent 7900). Analytical sequences included blanks, certified rock reference materials (BHVO-2, RGM-2, GSR-3, JA-2), and unknown samples for trace element quantification.

3. Results

3.1. Trace element composition of ferrihydrite substrates

Quantification of trace elements in the three types of Fh mineral particles with different initial trace element concentrations (0 ppm TE-Fh, 10 ppm TE-Fh and 20 ppm TE-Fh) revealed that most element concentrations ranged from 0 to 15 ppm (Table S2 and Fig. S2), and their levels generally increased with higher additions of the trace element stock solution. This indicates that the enrichment of most elements was directly proportional to the external input. Na, K, Ca, and Al exhibited elevated concentrations (0–~400 ppm), likely due to their stronger surface affinity for Fh, resulting in enhanced adsorption onto ferrihydrite surfaces, or their greater capacity to become incorporated into the ferrihydrite structure during mineral transformation. In contrast, Li, Mg, Sr, and Ag remained at low levels (0–~400 ppb) and reached saturation in the 20 ppm TE-Fh substrate, indicating limited binding capacity in Fh (Fig. S2).

3.2. Characterization of transformation mineral products

TEM observations showed that the magnetite products formed in both abiotic (Fig. 1a–c) and biotic (Fig. 1g–i) experiments were irregularly shaped. Particle sizes were quantified from ~900–1300 particles under each experimental condition using ImageJ. The average sizes of abiotic magnetite were 16.7 ± 7.8 nm for 0 ppm TE-Fh, 12.8 ± 7.4 nm for 10 ppm TE-Fh, and 9.7 ± 5.7 nm for 20 ppm TE-Fh (Fig. 1d–f), while the corresponding biogenic magnetite averaged 11.6 ± 9.2, 8.9 ± 4.8, and 7.1 ± 4.4 nm, respectively (Fig. 1j–l). At each trace-element level, biogenic magnetite was consistently smaller than its abiotic counterpart. Additionally, increasing trace element concentrations in the Fh substrates resulted in smaller magnetite nanoparticles in both abiotic and biotic systems. HRTEM of the final products (Fig. 1m–o), combined with subsequent Mössbauer spectroscopy, confirmed that magnetite was the dominant Fe-bearing mineral phase in all products.

Mössbauer spectra collected at 6 K for all samples were fitted with three sextets corresponding to the magnetite components: tetrahedral Fe^{3+} (Tet-site), octahedral Fe^{3+} (Oct-site), and octahedral Fe^{2+} (Oct-site) (Fig. 2 and Table S3). The hyperfine parameters of these subspectra fall within the ranges expected for well-crystallized magnetite, confirming that both abiotic and biotic treatments produced magnetite as the dominant Fe-bearing phase (Darbandi et al., 2012; Hah et al., 2021). Clear differences in Fe site distributions were observed between the abiotic and biogenic magnetite samples. In the abiotic products, the Oct-site Fe^{2+} population decreased systematically with increasing TE concentration, dropping from 38.3% at 0 ppm to 34.3% at 10 ppm and 26.7% at 20 ppm. Meanwhile, Fe^{3+} components exhibited an overall increase from 0 to 20 ppm. The Tet-site Fe^{3+} population increased from 40.3 to 45.6%, while the Oct-site Fe^{3+} fraction increased from 21.4 to 27.7%. This trend indicates a progressive shift toward a more oxidized magnetite as TE concentration increased in the abiotic experiment. The biogenic magnetite produced by *S. oneidensis* MR-1 showed a different behavior. The Oct-site Fe^{2+} fraction increased with increasing TE concentration, rising from 28.9% at 0 ppm to 37.3% at 10 ppm and 49.9% at 20 ppm. In contrast, the Tet-site Fe^{3+} population decreased markedly over the same range, from 49.6 to 42.8 and 31.5%, while the Oct-site Fe^{3+} fraction remained relatively similar, varying only slightly between 21.5, 20.0, and 18.7%. These variations in Fe valence distribution suggest that microbial Fe(III) reduction favors the formation of more reduced magnetite with increasing TE concentration. The Mössbauer spectra exhibit relatively high statistical noise, which mainly results from counting statistics associated with the limited absorber mass due to the low Fe concentration of the samples. Although the Mössbauer spectra were collected over a total acquisition period of two days to improve the signal-to-noise ratio, the spectral quality remained limited because of the small amount of Fe-bearing material available for analysis. Nevertheless, the spectra were sufficient for phase identification and quantitative fitting. The fitting quality was assessed using reduced χ^2 values (Table S3), and the 10% residual curves are provided in Fig. 2. Minor spectral broadening may be related to structural disorder associated with trace-element incorporation into magnetite. Although minor biomass-associated Fe species cannot be completely excluded in the biotic products, no additional spectral components were required for satisfactory fitting. Furthermore, the obtained hyperfine parameters are consistent with those reported for magnetite, and no resolvable spectral features indicative of ferrihydrite or other Fe-bearing phases were observed.

Additionally, Fe 2p XPS spectra and peak deconvolution of the transformation products formed under different conditions also exhibit characteristic Fe $2p_{3/2}$ and Fe $2p_{1/2}$ doublets accompanied by distinct satellite peaks (Fig. 3), indicating the coexistence of Fe^{2+} and Fe^{3+} species (Deng et al., 2025; Kumar et al., 2025). For the abiotic transformation products, the Fe(II) content determined by XPS ranges from 28.8 to 32.2%, while Fe(III) accounts for 67.8–71.2%. A slight increase in the Fe(III) fraction is observed with increasing initial trace element concentration of Fh substrates from 0 to 20 ppm. In contrast, the biotic transformation products induced by *S. oneidensis* MR-1 show relatively higher Fe(II) proportions compared to the abiotic counterparts. The XPS-derived Fe(II) fractions range from 33.8 to 36.7%, with corresponding Fe(III) contents of 63.3–66.2%. Although the Fe(II)/Fe(III) ratios obtained from XPS and Mössbauer spectroscopy are not identical, the XPS results show smaller variations in Fe(II) and Fe(III) contents in magnetite transformed from Fh substrates containing different trace-element concentrations compared with the Mössbauer data. The difference arises from the probing depths and principles of these two techniques. Mössbauer reflects bulk Fe valence and is sensitive to defects, causing larger Fe(II)/Fe(III) variation, while XPS probes only the near-surface region and may not fully represent bulk Fe valence heterogeneity (Byrne et al., 2016; Greczynski and Hultman, 2022). Nevertheless, both techniques consistently reveal the same overall trends: increasing trace-element concentrations in the Fh substrate promote higher Fe(III) proportions in abiotic magnetite, whereas they lead to increased Fe(II) proportions in biogenic magnetite.

3.3. Trace elements partitioning between solid products and its surrounding precipitation solution

Trace element concentrations for all fractions of transformation products are shown in Table S4. Results showed that all duplicates were consistent in all experimental conditions. The average standard deviation between two replicates is ~19% (RSD) with a median value around 11% (RSD). Based on Table S4, the transformation products exhibit wide concentration ranges of trace elements across different fractions and experimental conditions. The concentrations of five elements (Na, Mg, K, Ca and Al) in all fractions are higher and range over six orders of magnitude, from 10^1 to 10^7 ppb, whereas transition and heavy metals including Zn, Cu, Ni, Co, Mn, and Cr are present at intermediate concentrations of approximately 10^{-1}-10^2 ppb. In contrast, the other trace elements (Li, B, Ga, Sr, Ag, Cd, Ba, Tl, Pb, Bi) show relatively lower concentrations from 10^{-3} to 10^2 ppb. To quantify the relative incorporation of each element into solid products, a distribution coefficient (D^i) between solid products and their surrounding precipitation solution was calculated from the equation (1):

$$D^i = \frac{C^i_{solidproduct}}{C^i_{solution}} \quad (1)$$

where i is the kind of trace element, $C^i_{\text{solid product}}$ and C^i_{solution} are

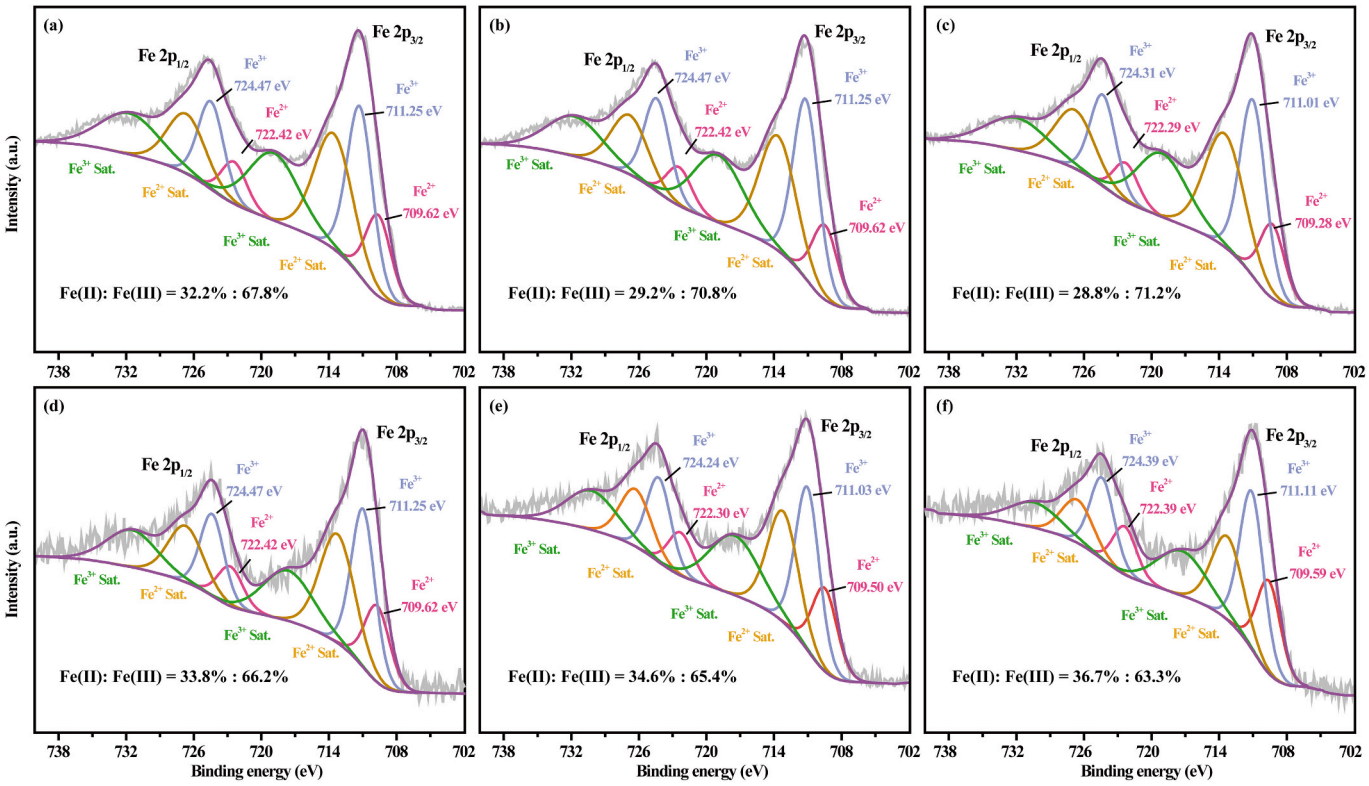


Fig. 3. XPS spectra and deconvolution for the Fe2p regions of transformation products induced by Fe^{2+}_{aq} abiotically (a-c) and *S. oneidensis* MR-1 biotically (d-f). (a)(d) show 0 ppm TE-Fh transformation products; (b)(e) show 10 ppm transformation products; (c)(f) are 20 ppm transformation products.

concentrations of an element *i* in solid products and their surrounding precipitation solution, respectively. In both abiotic and biotic experiments, the distribution coefficients of replicates are consistent between each other (Table S5, Fig. S3 and S4). Furthermore, D^i of each element was normalized with D^{Fe} of iron (equation (2)) to obtain their partition coefficients (K^i) which do not depend on the mass of magnetite.

$$K^i = \frac{D^i}{D^{Fe}} \tag{2}$$

Therefore, partition coefficients reflect the relative enrichment or depletion of trace elements in solid products: $K^i > 1$ or < 1 indicates an enrichment or depletion of this element (*i*) in solid products relative to iron.

K^i for solid fraction of transformation products without (Tp_{so}) and with NaAc ($Tp_{so\text{-}Ac}$) wash yielded consistent results (Fig. 4 and Table S6), suggesting NaAc did not affect trace element composition of the solid fraction. Overall, trace elements exhibit highly variable affinities for magnetite relative to the surrounding precipitation solution, depending on trace-element levels in the Fh substrate, trace element type and transformation pathway. The partition coefficients (K^i) for Tp_{so} and $Tp_{so\text{–}Ac}$ transformed from 0 ppm TE–Fh spanned a relatively narrow range of approximately 1×10^{-3} to 48. In contrast, the K^i values for Tp_{so} and Tp_{so}–Ac transformed from 10 ppm and 20 ppm TE–Fh exhibited much broader variability, extending from about 10^{-4} to 10^2. This broadened range is closely related to the increasing trace-element concentrations in the initial Fh mineral particles, which enhance elemental availability and promote more heterogeneous partitioning behavior during the Fh transformation to magnetite.

Under all conditions, K^K (10^{-4}–10^{-3}) and K^{Ga} (26–10^2) corresponded to the lowest and highest partition coefficients, respectively. The extremely low K^k values indicate that K is poorly incorporated into magnetite, which can be attributed to its large ionic radius and monovalent charge, making it energetically unfavorable for substitution into the magnetite crystal lattice dominated by divalent and trivalent cations. In contrast, Ga^{3+} has an ionic radius and charge more similar to Fe^{3+} under octahedral or tetrahedral coordination, facilitating its substitution into the spinel lattice. Consistent with this, Ga mapping in magnetite from ore samples shows that Ga can be incorporated via isomorphic substitution for Fe, explaining its relatively high partition coefficients (Ariëns et al., 2022; Weng et al., 2025). Additionally, Al, Cr, and Cd consistently showed $K^i > 1$ in the undoped systems, whereas Al, Cr, Cu, Zn, Pb, and Bi all exhibited $K^i > 1$ in the trace-element-doped systems (10 and 20 ppm). These values indicate preferential retention in magnetite-bearing solids relative to Fe, but do not establish lattice incorporation. Structural substitution, surface adsorption, and inheritance from the ferrihydrite precursor may all contribute, with biomass providing additional binding sites in the biotic systems, particularly for Cd, Pb, and Zn (Mishra et al., 2010; Wang et al., 2016; Yu and Fein, 2015).

Because $K^i > 1$ also occurred in cell-free abiotic experiments, it alone is not a biological signature. Comparing the partition coefficients of biogenic (K^i_B) and abiotic (K^i_A) products revealed contrasting trace-element retention (Fig. 4 and Table S7). Except for Co and Cd, most elements are more strongly depleted in biogenic products than in abiotic products. Notably, all K^{Co}_B/K^{Co}_A ratios exceed unity and remain relatively constant (~2–4) across mineralization products transformed from the three Fh substrates, indicating a robust enrichment of Co in biogenic products. An even more pronounced enrichment is observed for Cd, with K^{Cd}_B/K^{Cd}_A ratios consistently > 1 and reaching up to 94 for mineralization products transformed from 10 ppm TE-Fh. In contrast, Mg is the most strongly depleted element in biogenic products under all conditions, with K^{Mg}_A/K^{Mg}_B ratios reaching 174 at 10 ppm TE-Fh. These results suggest that Co and Cd are preferentially incorporated into biogenic products, whereas Mg is preferentially incorporated into abiotic products, and that these contrasting partitioning behaviors are largely independent of culture conditions, reflecting fundamental differences in mineral

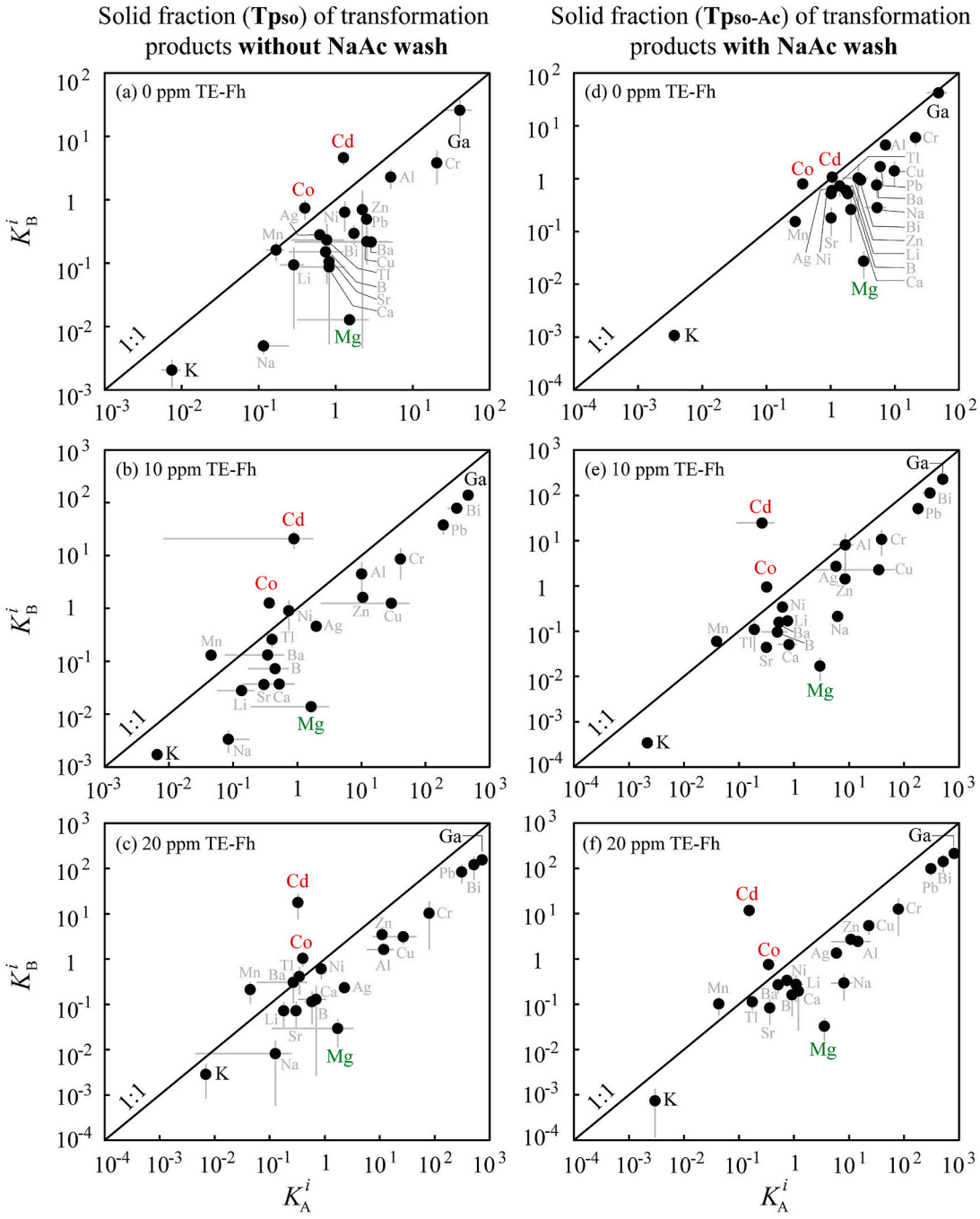


Fig. 4. Trace element partition coefficients for the solid fraction of Fh transformation products without (Tp_{so}) and with ($Tp_{so\text{-}Ac}$) NaAc wash in abiotic (K_A^i) and biotic (K_B^i) experiments. Except for Cd and Co, most elements are depleted in the biogenic magnetite produced by MR-1 compared with the abiotic magnetite (below the 1:1 line). Mg is the most depleted element in the biogenic magnetite compared with the abiotic magnetite.

formation pathways rather than environmental variability.

4. Discussion

4.1. Effects of trace elements and formation pathways on particle size of magnetite

Although Mössbauer spectroscopy is highly sensitive for identifying Fe-bearing mineral phases, minor amounts of residual Fe phases below the detection limit cannot be completely excluded. Nevertheless, the absence of detectable ferrihydrite signals in the Mössbauer spectra, together with the dominant magnetite morphology observed by HRTEM, indicates that magnetite was the primary transformation product. Across the three Fh mineral precursors, higher concentrations of trace elements produced progressively smaller magnetite particles in both abiotic and biotic experiments (Fig. 1). Generally, the adsorption of Fe^{2+} to Fh is necessary to induce Fh transformation to magnetite via solid-state conversion (Amstaetter et al., 2012; Han et al., 2020). Therefore, higher trace-element loadings likely reduce available reactive surface sites of Fh, leading to smaller particles of magnetite. This is supported by the previous study of Pb, where Pb loading blocks reactive surface sites on Fh, and lowers Fe^{2+} production, ultimately favoring the formation of finer magnetite crystals (Meite et al., 2022). Another plausible explanation is that trace elements enhance nucleation rates by

providing additional sites or lowering the energetic barrier for nucleation, while simultaneously inhibiting subsequent crystal growth through surface adsorption or partial incorporation into the magnetite lattice (Li et al., 2019; Watson, 1996). This is consistent with observations for lead (Pb) and arsenic (As), where Pb^{2+} and As(III) adsorb onto magnetite nuclei, reduce interfacial tension, and limit solute diffusion to the surface, thereby suppressing particle growth (Meite et al., 2022; Wang et al., 2008).

Biogenic magnetite was consistently smaller than its abiotic counterpart. This additional size control likely reflects microbial influences, including the involvement of cell surfaces, extracellular polymers, and enzymatic reduction processes, which create localized microenvironments that promote nucleation and restrict crystal enlargement (Dong et al., 2022; Han et al., 2024; Koepnick et al., 2025). Another reason could be due to the difference in total iron content between abiotic and biotic experiments. Although both systems started with 12 mM Fh, an additional 30 mM Fe^{2+} was supplied in abiotic experiments to promote Fh conversion, whereas in biotic experiments Fe^{2+} was produced only via microbial reduction (Piepenbrock et al., 2011). As a result, the abiotic system contained ~2.5 times more total iron, favoring larger particles. This is consistent with higher Fe concentrations in the final precipitates (~626 ppm in abiotic system vs. ~202 ppm in biotic system).

4.2. Structural heterogeneity and Fe valence states of magnetite

In addition to particle size effects, biogenic magnetite shows larger variations in isomer shift (δ) and quadrupole splitting (ΔE_Q) in Mössbauer spectra than abiotic magnetite for all three Fe components, especially octahedral Fe^{2+}, suggesting greater heterogeneity in local electronic density and coordination symmetry (Table S3). This greater heterogeneity can be linked to organic-influenced growth environments (Amstaetter et al., 2012). Previous studies demonstrate that organic molecules like L-cysteine can directly distort surface coordination, creating distinct Fe^{3+} species with altered δ, ΔE_Q, and smaller hyperfine magnetic fields (B_{hf}) (Iacob et al., 2025). Additionally, the B_{hf} of biogenic magnetite are generally lower or more variable than those of abiotic magnetite, suggesting weaker or less uniform magnetic exchange interactions. These features reflect the structurally heterogeneous nature of biogenic magnetite formed under microbially mediated conditions, where mineral nucleation and growth occur in spatially and chemically variable microenvironments. This is consistent with findings that organic impurities and nanoscale particle sizes, often promoted by organic electron shuttles, disrupt long-range magnetic order and induce superparamagnetic behavior, leading to spectral broadening (Markovski et al., 2017). In contrast, abiotic magnetite displays more uniform δ and ΔE_Q values and more stable B_{hf}. This spectral homogeneity reflects a more ordered spinel structure and homogeneous magnetic exchange, consistent with growth in a chemically uniform environment without strong organic-surface interactions (Shipilin et al., 2014).

Additionally, abiotic and biogenic magnetite exhibited opposite trends in Fe valence distributions with increasing concentrations of trace elements. In abiotic magnetite, decrease in Oct-site Fe^{2+} and enrichment of Fe^{3+} at both A and B sites indicate progressive oxidation with increasing trace-element incorporation. This trend arises because substituting cations (e.g., Mg^{2+}, Cu^{2+}, Ni^{2+}) preferentially occupy octahedral sites but do not participate in Fe^{2+}-Fe^{3+} electron hopping. As a result, charge compensation occurs via oxidation of neighboring Fe^{2+} and/or redistribution of Fe between A and B sites, leading to a lower Fe^{2+} fraction (Liang et al., 2013; Manohar and Krishnamoorthi, 2017; Melai et al., 2023). In contrast, biogenic magnetite exhibited enrichment of Oct-site Fe^{2+} and depletion of Tet-site Fe^{3+} with increasing trace element concentrations. This trend indicates that microbial Fe(III) reduction progressively favored the formation of more reduced magnetite, consistent with previous studies (Carvallo et al., 2008; Han et al., 2021). Moreover, trace elements likely enhance this process by acting as enzymatic cofactors or metabolic regulators that promote electron transfer in iron-reducing bacteria. Metals such as Cu, Ni, and Co support intracellular redox enzymes (Kunkle and Skaar, 2023; Mulrooney and Hausinger, 2003), while others (e.g., Cu^{2+}, Cd^{2+}, Ca^{2+}) can further stimulate extracellular electron transfer through shuttle production, improved cell adhesion, or cell aggregation (Fitzgerald et al., 2012; Xu et al., 2016). Together, these effects support a biologically dominated pathway in which trace elements enhance Fe(III) reduction and favor more reduced magnetite. Overall, abiotic and biogenic systems display distinct redox signatures and structural heterogeneity, reflecting their contrasting formation mechanisms.

4.3. Trace-element patterns in biogenic versus abiotic solid products

It should be noted that the solid fractions obtained after centrifugation may contain both magnetite particles and bacterial biomass in biotic experiments. Therefore, the measured elemental compositions may reflect contributions from mineral-associated pools as well as biological pools, including intracellular metals, cell-surface-bound metals, and extracellular polymeric substances (EPS)-associated metals. However, the objective of this study is to identify differences in trace element signatures between biogenic and abiotic magnetite formation pathways rather than to quantify elemental incorporation into the pure magnetite crystal lattice. Biological processes, including metal adsorption onto cell surfaces, EPS interactions, intracellular metal regulation, and biologically mediated mineral precipitation, are considered intrinsic components of biogenic mineral formation rather than analytical artifacts. The consistent differences observed between abiotic and biotic products reflect the combined effects of mineral formation pathways and biological processes, and these differences remain relevant for distinguishing biogenic from abiotic magnetite. ICP-MS results indicate that most trace elements are preferentially enriched in abiotic magnetite with Mg being the most enriched element in this group. In contrast, Co and Cd are consistently enriched in biogenic products, regardless of initial trace-element concentrations or washing treatments. Additionally, since K^i was normalized with iron, it should not vary with the yield of magnetite. The contrasting enrichment can be explained by differences in crystal-chemical substitution and biomineralization processes rather than environmental variability. In abiotic systems, Mg^{2+} (ionic radius 0.72 Å) closely matches Fe^{2+} (0.78 Å) and preferentially occupies the octahedral B sites in magnetite (Liu et al., 2022; Shannon, 1976). Rapid precipitation under cell-free conditions typically produces defect-rich and structurally open crystals (Dobrică et al., 2023), which further facilitate incorporation of small, high-affinity cations like Mg. Moreover, Mg is not directly involved in extracellular electron transfer by DIRB, limiting its interfacial enrichment during biomineralization (Lovley et al., 2004). Consistent with our observation of preferential Mg retention in abiotic products, Perez-Gonzalez et al. (2013) reported Mg incorporation into inorganic magnetite but not into magnetite produced by *Shewanella oneidensis*, suggesting that Mg incorporation depends on the mineral formation pathway.

In contrast, biogenic products formed by *S. oneidensis* MR-1 are enriched in Co and Cd due to strong interfacial adsorption and biological regulation. Co and Cd can interact with outer-membrane proteins and negatively charged functional groups (e.g., carboxyl and phosphoryl) on lipopolysaccharides and EPS (Sutherland et al., 2023; Wang et al., 2023). However, similar interactions may also occur for other transition metals, such as Cr and Cu, which are not significantly enriched in biogenic products. This suggests that trace-element incorporation is not controlled solely by surface adsorption, but may also depend on biological regulation of element uptake and detoxification processes. Essential elements are often tightly regulated and preferentially allocated to intracellular functions. In contrast, non-essential or toxic elements may accumulate through passive adsorption or detoxification mechanisms, increasing their potential incorporation into extracellular biogenic products. Moreover, Co can serve as a metabolic cofactor in

microorganisms (Kunkle and Skaar, 2023), but enhanced uptake related to this function is mainly expected under Co-limiting conditions. Because Co was supplied in our cultures, its role as a metabolic cofactor alone is unlikely to explain Co enrichment in biogenic products. While Cd can stimulate electron shuttle production (e.g., riboflavin) and cell adhesion, promoting extracellular electron transfer (Xu et al., 2016). These processes concentrate Cd during ferrihydrite reduction and magnetite nucleation, facilitating their incorporation. Furthermore, biologically controlled magnetite typically forms more slowly and with higher crystallographic order, favoring selective incorporation of transition metals over small alkaline-earth cations. Consequently, Co and Cd are more readily incorporated or surface-associated during the formation of biogenic products than Mg.

The Mössbauer-derived Fe^{2+}/Fe^{3+} ratios further support these mechanisms. At 0 ppm TE-Fh, abiogenic magnetite exhibits a higher Fe^{2+}/Fe^{3+} ratio (0.61) than biogenic magnetite (0.41). However, the trends diverge with increasing trace-element levels: abiogenic samples show a progressive decrease in Fe^{2+}/Fe^{3+} (0.52 at 10 ppm to 0.37 at 20 ppm), whereas biogenic samples display an increase (0.59 at 10 ppm and up to 1 at 20 ppm). This contrast is consistent with preferential Mg enrichment in abiogenic magnetite, where Mg^{2+} substitution for octahedral Fe^{2+} requires charge compensation through Fe^{2+} oxidation, thereby lowering the Fe^{2+} fraction (Melai et al., 2023). In contrast, biogenic magnetite is enriched in Co and Cd. Due to its variable valence and stronger electronic compatibility with the spinel lattice, Co can occupy both Fe^{2+} and Fe^{3+} sites in magnetite, therefore reducing the need for extensive Fe^{2+} oxidation by redistributing cations within the spinel structure (Byrne et al., 2013). Meanwhile, Cd^{2+} preferentially occupies tetrahedral Fe^{3+} sites owing to its relatively large ionic radius, thereby modifying the distribution of Fe^{3+} between tetrahedral and octahedral sites without altering the overall valence state (Bakeer et al., 2025). Consequently, the combined effects of Co and Cd incorporation in biogenic magnetite favor the retention of Fe^{2+} and the development of a more reduced magnetite structure compared with the Mg-enriched abiogenic counterpart.

Trace-element retention in the biogenic products may reflect contributions from both magnetite and associated biomass. Studies of biofilm-mineral interfaces demonstrate element-specific and condition-dependent partitioning. Wang et al. (2016) found that Zn(II) preferentially partitioned into *S. oneidensis* biofilms after short exposure, whereas Pb(II) favored reactive oxide surfaces at low concentrations and increasingly partitioned into biofilms at higher concentrations. Longer exposure increased mineral association for both elements. Templeton et al. (2001) likewise showed that mineral surfaces could dominate Pb (II) uptake despite the presence of biofilms. In contrast, Schmid et al. (2016) found that Ni was predominantly associated with iron minerals rather than organic constituents in cell-mineral aggregates. Although these systems differ from our magnetite-forming experiments, they demonstrate that biomass does not necessarily dominate trace-element retention. Our bulk analyses cannot uniquely assign Co or Cd enrichment to either magnetite or biomass and thus we interpret the partitioning as a property of the recovered biogenic solid products (i.e. cell-mineral aggregates) as a whole.

Overall, abiotic magnetite is controlled by crystal-chemical substitution that promotes Mg incorporation and Fe^{2+} oxidation, yielding a more oxidized state. In contrast, biogenic magnetite is governed by cell–mineral interactions that enrich Co and Cd and stabilize higher Fe^{2+} contents. The agreement among trace-element partitioning patterns, Mössbauer spectral parameters, and Fe^{2+}/Fe^{3+} ratios established a coherent mechanistic framework that links biomineralization pathways with the resulting chemical, structural and redox characteristics of magnetite.

4.4. Implications for the identification of biogenic magnetite in sediments

A comparison of the trace element composition of magnetite produced by DIRB in this study with that synthesized by MTB in previous studies (Amor et al., 2015; Mathon et al., 2024) reveals marked differences among *S. oneidensis* MR-1, *Magnetospirillum magneticum* AMB-1, and *Magnetovibrio blakemorei* MV-1 (Table S8 and Fig. 5). Magnetite produced by MR-1 exhibits systematically higher partition coefficients (K^i) than magnetite formed by magnetotactic bacteria, with enrichments of 1–5 orders of magnitude relative to AMB-1 and 1–4 orders of magnitude relative to MV-1 for most elements. The markedly elevated K^i values observed for MR-1 are consistent with extracellular magnetite precipitation, where trace elements can be incorporated through surface adsorption, coprecipitation, and lattice substitution (Crean et al., 2012; Sundman et al., 2020). In this setting, trace metals, particularly Cu, Ga, Cd, and Pb, are readily scavenged, resulting in enrichments of several orders of magnitude relative to intracellular magnetite. In contrast, magnetite formed by MTB (AMB-1 and MV-1) is produced intracellularly within magnetosome vesicles, where iron uptake, redox conditions, and crystal growth are tightly regulated (Lin et al., 2014; Wan et al., 2024). This strong biological control leads to systematic exclusion of most trace elements, yielding uniformly low K^i values in AMB-1. The intermediate behavior of MV-1 likely stems from its maintenance of higher intracellular concentrations of these elements compared to AMB-1. This difference originates from the distinct properties of their efflux pump systems (Mathon et al., 2024). Consequently, a greater amount of trace elements is incorporated into magnetite by MV-1 than by AMB-1, though still far less than by MR-1. In addition, the higher concentrations of trace elements observed in the abiotic magnetite produced in this study, compared to those reported for the abiotic counterpart of MTB magnetite, can be attributed to differences in formation pathways. The latter is synthesized via the co-precipitation of Fe^{3+}_{aq} and Fe^{2+}_{aq} ions in the presence of trace elements. In contrast, the magnetite in our system is predominantly formed through the Fe^{2+}_{aq}-induced solid-state transformation of ferrihydrite, which retains substrate-associated elements. Overall, trace-element signatures in magnetite are strongly controlled by formation pathway, suggesting magnetite trace element compositions could be indicators of microbial processes in modern and ancient environments.

The results of this study provide new insights into how trace elements, Fe valence states, and structural characteristics can be used to distinguish magnetite formed through different pathways, with important implications for identifying biogenic magnetite in natural and

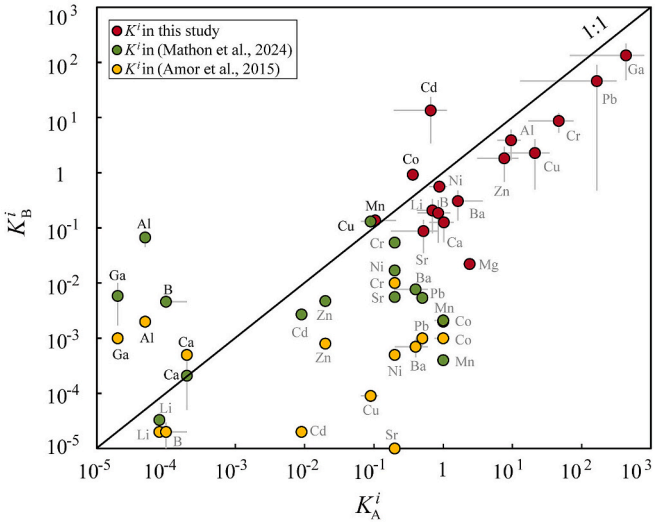


Fig. 5. A comparison of the trace element composition of magnetite produced by DIRB in this study with that synthesized by MTB in previous studies (Amor et al., 2015; Mathon et al., 2024). The K^i values from this study represent the average values obtained from experiments conducted under three TE-Fh conditions (0, 10, and 20 ppm TE-Fh).

ancient sedimentary environments. First, biogenic magnetite formed by *S. oneidensis* MR-1 consistently exhibits smaller particle sizes and greater Mössbauer spectral variability than abiotic magnetite. These features likely reflect the heterogeneous microenvironments created at cell–mineral interfaces, where extracellular polymers, cell surfaces, and enzymatic reduction processes regulate nucleation and growth. Although particle size alone cannot serve as a definitive biosignature due to possible overlap with abiotic nanoparticles, the combination of nanoscale size distributions with enhanced structural heterogeneity may provide supportive evidence for microbially mediated formation. In addition, the contrasting Fe valence trends between abiotic and biogenic systems represent an additional diagnostic feature. In abiotic magnetite, increasing trace-element concentrations lead to progressive Fe^{2+} depletion and Fe^{3+} enrichment, while biogenic magnetite shows the opposite behavior, with increasing Fe^{2+} enrichment driven by microbial Fe(III) reduction. This divergence reflects fundamentally different redox controls during mineral formation and suggests that Fe valence distributions in magnetite could serve as a complementary proxy for identifying microbially mediated mineralization pathways in sediments.

Furthermore, and most importantly, trace-element partitioning patterns provide a robust geochemical fingerprint of magnetite formation pathways. Among the analyzed elements, Mg, Co, and Cd exhibit the most systematic differences between abiotic and biogenic products. Mg is strongly enriched in abiotic magnetite, with partition coefficients (K^{Mg}) ranging from ~1.5 to 3.6, whereas biogenic products produced by *S. oneidensis* MR-1 show extremely low Mg incorporation (K^{Mg}≈0.01–0.03). In contrast, Co and Cd are consistently enriched in biogenic products relative to abiotic samples. The most pronounced difference is observed for Cd, whose partition coefficients (K^{Cd}) in biogenic products exceed those of abiotic products by up to two orders of magnitude. Because fluid compositions in ancient sedimentary systems are generally difficult to constrain, partition coefficient ratios rather than raw partition coefficient values may provide more practical indicators of mineral origin. Unlike Mg, Co, and Cd, Mn exhibits broadly similar partitioning behavior in both abiotic (K^{Mn} = 0.04–0.28) and biotic (K^{Mn} = 0.06–0.21) systems, making it a suitable reference element for constructing partition coefficient ratios that are less sensitive to variations in fluid composition. Although the use of Mn as a reference eliminates the need to constrain Mn concentrations in the parent fluid, independent estimates of Mg and Cd concentrations in the fluid are still required when applying these ratios to natural samples. In practice, the required fluid compositions may be constrained using coexisting minerals that equilibrated with the same fluid, such as carbonates associated with magnetite (Mathon et al., 2024), thereby improving the applicability of these partition coefficient ratios to natural rock samples. Based on this study, the K^{Mg}/K^{Mn} and K^{Cd}/K^{Mn} ratios show clear contrast between abiotic and biogenic products. Abiotic products typically exhibit K^{Mg}/K^{Mn} ratios of approximately 10–80, whereas biogenic products show much lower values of about 0.08–0.3, corresponding to a difference of roughly two to three orders of magnitude. This large difference indicates that the K^{Mg}/K^{Mn} ratio is an effective indicator for identifying chemically formed magnetite. In contrast, the K^{Cd}/K^{Mn} ratio is more characteristic of DIRB-generated biogenic products. Abiotic products generally show K^{Cd}/K^{Mn} ratios of about 3–20, whereas biogenic products exhibit significantly higher values of approximately 10–400, representing a difference of about one to two orders of magnitude. Such enrichment in Cd relative to Mn provides an additional geochemical criterion for recognizing magnetite of biological origin. Because the partition coefficients are normalized to iron, they are largely independent of magnetite yield and therefore provide a reliable indicator of formation mechanisms. The reproducible enrichment patterns of Mg and Cd across different trace-element concentrations and washing treatments suggest that these elements may serve as particularly useful markers for distinguishing DIRB-derived magnetite from abiotic magnetite in sedimentary records.

Magnetite commonly occurs together with Fe-Mn nodules, iron (oxyhydr)oxides, clay minerals, and carbonates in sedimentary environments, which may provide indirect constraints on the trace-element composition of the fluids present during mineral formation (Mathon et al., 2024). Even if the composition of the ancient fluid phase can only be estimated within one order of magnitude, the large differences in K^{Mg}/K^{Mn} and K^{Cd}/K^{Mn} ratios observed here should still allow discrimination between abiotic and microbially mediated magnetite formation. Taken together, these results demonstrate that no single parameter is sufficient to identify biogenic magnetite in sediments. Instead, a multiproxy approach combining trace element partitioning patterns, Fe valence distributions, and structural characteristics provides a more reliable framework for recognizing magnetite formed through microbial processes. Application of such integrated geochemical and mineralogical criteria to magnetite-bearing sedimentary rocks may therefore provide a useful tool for identifying extracellular magnetite produced by dissimilatory Fe(III)-reducing bacteria in both modern environments and the geological record.

5. Conclusions

We cultivated a DIRB (*Shewanella oneidensis* MR-1) with Fh containing various amounts of trace elements to test possible generalization of this proxy for identification of biogenic magnetite. Results demonstrate that the microbially formed magnetite retains a strong geochemical memory of its formation pathway (compared to abiotic transformation of Fh to magnetite), expressed through systematic differences in crystal chemistry and trace-element behavior. In abiotic systems, trace-element incorporation is governed primarily by lattice substitution and charge-compensation mechanisms, leading to progressive modification of Fe site occupancy and a shift toward more oxidized compositions as trace element concentrations increase. In contrast, magnetite formed by Fe(III)-reducing bacteria reflects biologically regulated interfacial processes in which microbial Fe(III) reduction, localized redox conditions, and surface complexation collectively shape mineral composition. The preferential enrichment of Mg in abiotic products and Co–Cd in biogenic products highlights the contrasting controls of crystal-chemical versus biologically mediated processes. In addition to trace-element partitioning, our results also demonstrate that biogenic magnetite is characterized by a more reduced Fe valence state than abiotic magnetite. Moreover, comparison with MTB magnetite emphasizes that the degree and mode of biological control fundamentally determine trace-element partitioning patterns. Integrating multielement partitioning with structural parameters therefore provides a robust framework for identifying extracellular microbial magnetite. These findings advance the mechanistic basis for interpreting magnetite compositions in modern and ancient environments and strengthen the use of trace-element systematics as indicators of ancient iron-reducing activity on Earth and, by analogy, in extraterrestrial settings where magnetite is preserved.

Data availability

Data are available through Mendeley Data at: https://data.mendeley.com/datasets/3f537pmp6n/1.

CRediT authorship contribution statement

Xiaohua Han: Writing – original draft, Visualization, Validation, Methodology, Investigation, Funding acquisition, Formal analysis, Data curation, Conceptualization. **James M. Byrne:** Writing – review & editing, Formal analysis. **Andreas Kappler:** Writing – review & editing, Conceptualization. **Wei Lin:** Writing – review & editing, Funding acquisition. **Yongxin Pan:** Writing – review & editing, Funding acquisition.

Declaration of competing interest

The authors declare that they have no known competing financial interests or personal relationships that could have appeared to influence the work reported in this paper.

Acknowledgments

This research was funded by the National Natural Science Foundation of China (Grant No. 42388101, 42293293, 42574082, 42204085). We would like to thank Yan Liu and Xu Tang for assistance in TEM analyses, and Leri Ge for Mössbauer spectroscopic analysis.

Appendix A. Supplementary material

Supplementary material to this article can be found online at https://doi.org/10.1016/j.gca.2026.10.037.

References

Amor, M., Busigny, V., Duranddubief, M., Tharaud, M., Onanguema, G., Gélabert, A., Alphandéry, E., Menguy, N., Benedetti, M.F., Chebbi, I., 2015. Chemical signature of magnetotactic bacteria. PNAS 112, 1699–1703.

Amor, M., Busigny, V., Louvat, P., Gélabert, A., Cartigny, P., Durand-Dubief, M., Ona-Nguema, G., Alphandéry, E., Chebbi, I., Guyot, F., 2016. Mass-dependent and -independent signature of Fe isotopes in magnetotactic bacteria. Science 352, 705–708.

Amstaetter, K., Borch, T., Kappler, A., 2012. Influence of humic acid imposed changes of ferrihydrite aggregation on microbial Fe(III) reduction. Geochim. Cosmochim. Acta 85, 326–341.

Ariëns, M.I., van de Water, L.G.A., Dugulan, A.I., Brück, E., Hensen, E.J.M., 2022. Substituting Chromium in Iron-based Catalysts for the High-Temperature Water–Gas Shift Reaction. ACS Catal. 12, 13838–13852.

Bakeer, D.E.S., Sayed, M.Y.E., Abdallah, E.M., Awad, R., Elsharkawy, S.G., 2025. Structural and magnetic tailoring of Co-Cu ferrite nanoparticles via Cd2+ substitution: a multi-characterization approach. Appl. Phys. A 131.

Byrne, J., Coker, V., Moise, S., Wincott, P., Vaughan, D., Tuna, F., Arenholz, E., Van Der Laan, G., Pattrick, R., Lloyd, J., 2013. Controlled cobalt doping in biogenic magnetite nanoparticles. J. R. Soc. Interface 10, 20130134.

Byrne, J.M., Van Der Laan, G., Figueroa, A.I., Qafoku, O., Wang, C., Pearce, C.I., Jackson, M., Feinberg, J., Rosso, K.M., Kappler, A., 2016. Size dependent microbial oxidation and reduction of magnetite nano-and micro-particles. Sci. Rep. 6, 30969.

Carvallo, C., Sainctavit, P., Arrio, M., Menguy, N., Wang, Y., Ona-Nguema, G., Brice-Profeta, S., 2008. Biogenic vs. abiogenic magnetite nanoparticles: a XMCD study. Am. Miner. 93, 880–885.

Crean, D.E., Coker, V.S., van der Laan, G., Lloyd, J.R., 2012. Engineering biogenic magnetite for sustained Cr(VI) remediation in flow-through systems. Environ. Sci. Technol. 46, 3352–3359.

Crosby, H.A., Johnson, C.M., Roden, E.E., Beard, B.L., 2005. Coupled Fe(II)−Fe(III) Electron and Atom Exchange as a Mechanism for Fe Isotope Fractionation during Dissimilatory Iron Oxide Reduction. Environ. Sci. Technol. 39, 6698–6704.

Crosby, H.A., Roden, E.E., Johnson, C.M., Beard, B.L., 2007. The mechanisms of iron isotope fractionation produced during dissimilatory Fe(III) reduction by Shewanella putrefaciens and Geobacter sulfurreducens. Geobiology 5, 169–189.

Darbandi, M., Stromberg, F., Landers, J., Reckers, N., Sanyal, B., Keune, W., Wende, H., 2012. Nanoscale size effect on surface spin canting in iron oxide nanoparticles synthesized by the microemulsion method. J. Phys. D Appl. Phys. 45, 195001.

Deng, S., Ma, Y., Han, Y., Zhou, Q., Fu, W., 2025. Exploring the peroxidase-like activity of 4Fe–Ni–B nanoparticles for analytical sensing. RSC Adv. 15, 7535–7545.

Dobrică, E., Ishii, H.A., Bradley, J.P., Ohtaki, K., Brearley, A.J., Noguchi, T., Matsumoto, T., Miyake, A., Igami, Y., Haruta, M., Saito, H., Hata, S., Seto, Y., Miyahara, M., Tomioka, N., Leroux, H., Le Guillou, C., Jacob, D., de la Peña, F., Laforet, S., Marinova, M., Langenhorst, F., Harries, D., Beck, P., Phan, T.H.V., Rebois, R., Abreu, N.M., Gray, J., Zega, T., Zanetta, P., Thompson, M.S., Stroud, R., Burgess, K., Cymes, B.A., Bridges, J.C., Hicks, L., Lee, M.R., Daly, L., Bland, P.A., Zolensky, M.E., Frank, D.R., Martinez, J., Tsuchiyama, A., Yasutake, M., Matsuno, J., Okumura, S., Mitsukawa, I., Uesugi, K., Uesugi, M., Takeuchi, A., Sun, M., Enju, S., Takigawa, A., Michikami, T., Nakamura, T., Matsumoto, M., Nakauchi, Y., Yurimoto, H., Okazaki, R., Yabuta, H., Naraoka, H., Sakamoto, K., Tachibana, S., Yada, T., Nishimura, M., Nakato, A., Miyazaki, A., Yogata, K., Abe, M., Okada, T., Usui, T., Yoshikawa, M., Saiki, T., Tanaka, S., Terui, F., Nakazawa, S., Watanabe, S., Tsuda, Y., 2023. Nonequilibrium spherulitic magnetite in the Ryugu samples. Geochim. Cosmochim. Acta 346, 65–75.

Dong, H., Huang, L., Zhao, L., Zeng, Q., Liu, X., Sheng, Y., Shi, L., Wu, G., Jiang, H., Li, F., Zhang, L., Guo, D., Li, G., Hou, W., Chen, H., 2022. A critical review of mineral–microbe interaction and co-evolution: mechanisms and applications. Natl. Sci. Rev. 9, nwac128.

Fitzgerald, L.A., Petersen, E.R., Gross, B.J., Soto, C.M., Ringeisen, B.R., El-Naggar, M.Y., Biffinger, J.C., 2012. Aggrandizing power output from Shewanella oneidensis MR-1 microbial fuel cells using calcium chloride. Biosens. Bioelectron. 31, 492–498.

Greczynski, G., Hultman, L., 2022. A step-by-step guide to perform x-ray photoelectron spectroscopy. J. Appl. Phys. 132, 011101.

Hah, H.Y., Gray, S., Johnson, C.E., Johnson, J.A., Kolesnichenko, V., Kucheryavy, P., Goloverda, G., 2021. Mössbauer spectroscopy of superparamagnetic Fe3O4 nanoparticles. J. Magn. Magn. Mater. 539, 168382.

Han, X., Pan, Y., 2024. Mineralization products of iron-reducing bacteria and their implications to Iron Formations deposition. Acta Petrol. Sin. 40 (4), 1299–1310.

Han, X., Tomaszewski, E.J., Schoenberg, R., Konhauser, K.O., Amor, M., Pan, Y., Warter, V., Kappler, A., Byrne, J.M., 2021. Using Zn and Ni behavior during magnetite precipitation in banded iron formations to determine its biological or abiotic origin. Earth Planet. Sci. Lett. 568, 117052.

Han, X., Tomaszewski, E.J., Sorwat, J., Pan, Y., Kappler, A., Byrne, J.M., 2020. Effect of Microbial Biomass and Humic Acids on Abiotic and Biotic Magnetite Formation. Environ. Sci. Technol. 54, 4121–4130.

Han, X., Wang, F., Zheng, S., Qiu, H., Liu, Y., Wang, J., Menguy, N., Leroy, E., Bourgon, J., Kappler, A., Liu, F., Pan, Y., Li, J., 2024. Morphological, Microstructural, and In Situ Chemical Characteristics of Siderite Produced by Iron-reducing Bacteria. Environ. Sci. Technol. 58, 11016–11026.

Hua, Y., Ren, G., Li, H., Wang, Q., Tarduno, J.A., Huang, J., Liu, C., Yang, Y., Wang, R., Yang, X., Han, X., Pan, Y., He, H., Nie, J., 2026. A new mechanism for magnetite formation in loess. Sci. Bull. 71 (9), 2348–2354.

Iacob, N., Palade, P., Comanescu, C., Crisan, O., Toderascu, L.I., Socol, G., Schinteie, G., Kuncser, V., 2025. Comprehensive Methodology for evaluating the Drug Loading of Iron Oxide Nanoparticles using combined Magnetometry and Mössbauer Spectroscopy. Molecules 30, 676.

Koepnick, H.R., Peyton, B.M., Lauchnor, E.G., 2025. Nitrate-dependent iron oxidation for bioremediation of metal, metalloid, and radionuclide contaminants. Rev. Environ. Sci. Bio-Technol. 24, 661–694.

Kumar, Y.R., Trivedi, P., Jana, A., Suman, D., Vasundhara, M., 2025. Preparation of biotemplated Fe3O4 nanoparticles and evaluation of RF-induced heating efficiency for targeted hyperthermia. RSC Adv. 15, 36879–36894.

Kunkle, D.E., Skaar, E.P., 2023. Moving metals: how microbes deliver metal cofactors to metalloproteins. Mol. Microbiol. 120, 547–554.

Li, T., Xie, Y., Wang, X., Shen, Q., Li, J., Guo, H., Xu, J., Liu, W., 2019. Mn promotes the rate of nucleation and growth of precipitates by increasing Frenkel pairs in Fe–Cu based alloys. RSC Adv. 9, 19620–19629.

Liang, X., Zhong, Y., Zhu, S., He, H., Yuan, P., Zhu, J., Jiang, Z., 2013. The valence and site occupancy of substituting metals in magnetite spinel structure Fe3−xMxO4 (M = Cr, Mn, Co and Ni) and their influence on thermal stability: an XANES and TG-DSC investigation. Solid State Sci. 15, 115–122.

Lin, W., Bazylinski, D.A., Xiao, T., Wu, L.F., Pan, Y., 2014. Life with compass: diversity and biogeography of magnetotactic bacteria. Environ. Microbiol. 16, 2646–2658.

Lin, W., Paterson, G.A., Zhu, Q., Wang, Y., Kopylova, E., Li, Y., Knight, R., Bazylinski, D. A., Zhu, R., Kirschvink, J.L., 2017. Origin of microbial biomineralization and magnetotaxis during the Archean. PNAS 114, 2171–2176.

Liu, Y., Li, X., Yang, X., Chang, S., Feng, J., Li, X., Zhu, X., Zong, Y., Liu, X., Zheng, X., 2022. Nonmagnetic Mg2+-induced cation occupation and magnetic properties of magnetite nanocrystals. J. Mater. Sci.-Mater. Electron. 33, 5587–5598.

Lovley, D.R., Holmes, D.E., Nevin, K.P., 2004. Dissimilatory Fe (III) and Mn (IV) reduction. Adv. Microb. Physiol. 49, 219–286.

Manohar, A., Krishnamoorthi, C., 2017. Site selective Cu2+ substitution in single crystal Fe3O4 biocompatible nanospheres by solvothermal reflux method. J. Cryst. Growth 473, 66–74.

Markovski, C., Byrne, J.M., Lalla, E., Lozano-Gorrín, A.D., Klingelhöfer, G., Rull, F., Kappler, A., Hoffmann, T., Schröder, C., 2017. Abiotic versus biotic iron mineral transformation studied by a miniaturized backscattering Mössbauer spectrometer (MIMOS II), X-ray diffraction and Raman spectroscopy. Icarus 296, 49–58.

Mathon, F.P., Amor, M., Guyot, F., Menguy, N., Lefevre, C.T., Busigny, V., 2024. Establishing the content in trace and minor elements of magnetite as a biosignature of magnetotactic bacteria. Geochim. Cosmochim. Acta 386, 127–138.

Meite, F., Hauet, T., Billard, P., Ferté, T., Abdelmoula, M., Zegeye, A., 2022. Insight into the magnetic properties of Pb-dopped iron oxide nanoparticles during Fe(III) bio-reduction by Shewanella oneidensis MR-1. Chem. Geol. 606, 120904.

Melai, C., Boffa Ballaran, T., Uenver-Thiele, L., Kurnosov, A., Chumakov, A.I., Bessas, D., Frost, D.J., 2023. Compressibilities along the magnetite–magnesioferrite solid solution. Phys. Chem. Miner. 50, 1.

Mishra, B., Boyanov, M., Bunker, B.A., Kelly, S.D., Kemner, K.M., Fein, J.B., 2010. High- and low-affinity binding sites for Cd on the bacterial cell walls of *Bacillus subtilis* and Shewanella oneidensis. Geochim. Cosmochim. Acta 74, 4219–4233.

Moskowitz, B.M., Frankel, R.B., Bazylinski, D.A., 1993. Rock magnetic criteria for the detection of biogenic magnetite. Earth Planet. Sci. Lett. 120, 283–300.

Mulrooney, S.B., Hausinger, R.P., 2003. Nickel uptake and utilization by microorganisms. FEMS Microbiol. Rev. 27, 239–261.

Perez-Gonzalez, T., Valverde-Tercedor, C., Yebra-Rodriguez, A., Prozorov, T., Gonzalez-Muñoz, M.T., Arias-Peñalver, J.M., Jimenez-Lopez, C., 2013. Chemical Purity of Shewanella oneidensis-Induced Magnetites. Geomicrobiol J. 30, 731–748.

Pérez-Huerta, A., Cappelli, C., Jabalera, Y., Prozorov, T., Jimenez-Lopez, C., Bazylinski, D.A., 2022. Biogeochemical fingerprinting of magnetotactic bacterial magnetite. PNAS 119, e2203758119.

Piepenbrock, A., Dippon, U., Porsch, K., Appel, E., Kappler, A., 2011. Dependence of microbial magnetite formation on humic substance and ferrihydrite concentrations. Geochim. Cosmochim. Acta 75, 6844–6858.

Raven, K.P., Jain, A., Loeppert, R.H., 1998. Arsenite and Arsenate Adsorption on Ferrihydrite: Kinetics, Equilibrium, and Adsorption Envelopes. Environ. Sci. Technol. 32, 344–349.

Schmid, G., Zeitvogel, F., Hao, L., Ingino, P., Adaktylou, I., Eickhoff, M., Obst, M., 2016. Submicron-scale heterogeneities in nickel sorption of various cell-mineral aggregates formed by Fe(II)-oxidizing bacteria. Environ. Sci. Technol. 50, 114–125.
Schröder, I., Johnson, E., de Vries, S., 2003. Microbial ferric iron reductases. FEMS Microbiol. Rev. 27, 427–447.
Shannon, R.D., 1976. Revised effective ionic radii and systematic studies of interatomic distances in halides and chalcogenides. Acta Crystallographica Section A 32, 751–767.
Shipilin, M., Zakharova, I., Shipilin, A., Bachurin, V., 2014. Mössbauer studies of magnetite nanoparticles. J. Surf. Ingestig.-X-Ray Synchro. 8, 557–561.
Sundman, A., Vitzthum, A.-L., Adaktylos-Surber, K., Figueroa, A.I., van der Laan, G., Daus, B., Kappler, A., Byrne, J.M., 2020. Effect of Fe-metabolizing bacteria and humic substances on magnetite nanoparticle reactivity towards arsenic and chromium. J. Hazard. Mater. 384, 121450.
Sutherland, C., Chittoo, B.S., Samlal, A., 2023. The status of scientific development on the application of biosorption of heavy metals at laboratory and pilot-scale: a review. Desalin. Water Treat. 299, 13–49.
Templeton, A.S., Trainor, T.P., Traina, S.J., Spormann, A.M., Brown Jr., G.E., 2001. Pb (II) distributions at biofilm-metal oxide interfaces. PNAS 98, 11897–11902.
Wan, J., Ji, R., Liu, J., Ma, K., Pan, Y., Lin, W., 2024. Biomineralization in magnetotactic bacteria: from diversity to molecular discovery-based applications. Cell Rep. 43.
Wang, Y., Gélabert, A., Michel, F.M., Choi, Y., Gescher, J., Ona-Nguema, G., Eng, P.J., Bargar, J.R., Farges, F., Spormann, A.M., Brown, G.E., 2016. Effect of biofilm coatings at metal-oxide/water interfaces I: Pb(II) and Zn(II) partitioning and speciation at Shewanella oneidensis/metal-oxide/water interfaces. Geochim. Cosmochim. Acta 188, 368–392.
Wang, Y., Morin, G., Ona-Nguema, G., Menguy, N., Juillot, F., Aubry, E., Guyot, F., Calas, G., Brown, G.E., 2008. Arsenite sorption at the magnetite–water interface during aqueous precipitation of magnetite: EXAFS evidence for a new arsenite surface complex. Geochim. Cosmochim. Acta 72, 2573–2586.
Wang, Z., Tan, R., Gong, J., Gong, B., Guan, Q., Mi, X., Deng, D., Liu, X., Liu, C., Deng, C., 2023. Process parameters and biological mechanism of efficient removal of Cd (II) ion from wastewater by a novel *Bacillus subtilis* TR1. Chemosphere 318, 137958.
Watson, E.B., 1996. Surface enrichment and trace-element uptake during crystal growth. Geochim. Cosmochim. Acta 60, 5013–5020.
Weng, X., Meng, Y., Huang, X., Shang, L., Hu, R., Bi, X., 2025. Ga- and Ge-bearing minerals and trace element-rich magnetite in the Makeng skarn Fe polymetallic deposit, Eastern China. J. Asian Earth Sci. 291, 106683.
Wu, L., Beard, B.L., Roden, E.E., Johnson, C.M., 2009. Influence of pH and dissolved Si on Fe isotope fractionation during dissimilatory microbial reduction of hematite. Geochim. Cosmochim. Acta 73, 5584–5599.
Wu, W.F., Wang, F.P., Li, J.H., Yang, X.W., Xiao, X., Pan, Y.X., 2013. Iron reduction and mineralization of deep-sea iron reducing bacterium Shewanella piezotolerans WP3 at elevated hydrostatic pressures. Geobiology 11, 593–601.
Xu, Y.S., Zheng, T., Yong, X.Y., Zhai, D.D., Si, R.W., Li, B., Yu, Y.Y., Yong, Y.C., 2016. Trace heavy metal ions promoted extracellular electron transfer and power generation by Shewanella in microbial fuel cells. Bioresour. Technol. 211, 542–547.
Yu, Q., Fein, J.B., 2015. The effect of metal loading on Cd adsorption onto Shewanella oneidensis bacterial cell envelopes: the role of sulfhydryl sites. Geochim. Cosmochim. Acta 167, 1–10.